Du, Ruifeng; Xiao, Ke; Li, Baoying; [et al.]. «Controlled oxygen doping in highly dispersed Ni-loaded g-C3N4 nanotubes for efficient photocatalytic H2O2 production». Chemical engineering journal, Vol. 441 (Aug. 2022), art. 135999. DOI 10.1016/j.cej.2022.135999

Controlled oxygen doping in highly dispersed Ni-loaded g-C_3N_4 nanotubes for efficient photocatalytic H_2O_2 production

Ruifeng Du[a,b], Ke Xiao[a,b], Baoying Li [c,*], Xu Han[d], Chaoqi Zhang[a,b], Xiang Wang[a,b], Yong Zuo[a,e], Pablo Guardia[a], Junshan Li[f], Jianbin Chen[c,*], Jordi Arbiol[d,g], Andreu Cabot[a,g,*]

[a] Catalonia Energy Research Institute - IREC, Sant Adrià de Besòs, 08930 Barcelona, Spain

[b] Departament d'Enginyeria Electrònica i Biomèdica, Universitat de Barcelona, 08028, Barcelona, Spain

[c] Shandong Provincial Key Laboratory of Molecular Engineering, State Key Laboratory of Biobased Material and Green Papermaking, School of Chemistry and Chemical Engineering, Qilu University of Technology, Shandong Academy of Sciences, Jinan, 250353, P. R. China

[d] Catalan Institute of Nanoscience and Nanotechnology (ICN2), CSIC and BIST, Campus UAB, Bellaterra, 08193, Barcelona, Catalonia, Spain

[e] Istituto Italiano di Tecnologia, Via Morego 30, Genova, 16163 Italy

[f] Institute of Advanced Study, Chengdu University, Chengdu 610106, China

[g] ICREA, Pg. Lluis Companys 23, 08010 Barcelona, Catalonia, Spain.

Abstract

Hydrogen peroxide (H_2O_2) is both a key component in several industrial processes and a promising liquid fuel. H_2O_2 can be produced by solar photocatalysis as a suitable strategy to convert and store solar energy into chemical energy. Here we report an oxygen-doped tubular g-C_3N_4 with uniformly dispersed nickel nanoparticles for efficient photocatalytic H_2O_2 generation. The hollow structure of the tubular g-C_3N_4 provides a large surface with a high density of reactive sites and efficient visible light absorption during photocatalytic reaction. The oxygen doping and Ni loading enable a fast separation of photogenerated charge carriers and a high selectivity toward the two-electron process during the oxygen reduction reaction (ORR). The optimized composition, $Ni_{4\%}/O_{0.2}$tCN, displays an H_2O_2 production rate of 2464 μmol $g^{-1}\cdot h^{-1}$, which is eightfold higher than that of bulk g-C_3N_4 under visible light irradiation (λ > 420 nm), and achieves an apparent quantum yield (AQY) of 28.2% at 380 nm and 14.9% at 420 nm.

Keywords: carbon nitride; nanotubes; nickel nanoparticles; photocatalysis, H_2O_2

1. Introduction

Hydrogen peroxide is an important industrial raw material used among others as an eco-friendly oxidant for industrial synthesis, pulp bleaching and wastewater treatment, with a global annual demand of over 4 million tons.[1–4] Besides, H_2O_2 is also a promising liquid fuel that is safer and easier to store than compressed hydrogen.[5,6] At present, H_2O_2 is industrially produced mainly through the anthraquinone method, which is an energy-intensive process requiring large amounts of organic solvent.[7] Therefore, the development of cost-effective and environmentally friendly strategies for the large scale production of H_2O_2 is a worthwhile endeavour. In this scenario, the production of H_2O_2 using solar photocatalysis has received increased attention in recent years.[8,9]

Several photocatalysts have been applied for H_2O_2 generation, including titanium dioxide[10,11], graphitic carbon nitride (g-C_3N_4)[12,13] and bismuth vanadate[14], to cite a few. Among them, g-C_3N_4 is particularly interesting as a metal-free, non-toxic and chemically stable material that has shown excellent potential not only for H_2O_2 generation but also for hydrogen generation and wastewater treatment, among others. However, the low surface area, moderate light absorption, rapid recombination of the photogenerated electron-hole pairs and low photocatalytic reaction selectivity towards H_2O_2 generation limits the cost-effective use of g-C_3N_4 for photocatalytic H_2O_2 production. To overcome these limitations, several strategies have been developed, including tuning the g-C_3N_4 morphology, extrinsically doping it, and forming heterojunctions through the loading of a co-catalyst.[15–19]

It is well known that the morphology and nanostructure of g-C_3N_4 largely affect its photocatalytic performance. To date, several g-C_3N_4 morphologies, such as nanosheets,[20] nanospheres,[21] nanorods,[22] nanofibers[23] and nanotubes[24] have been prepared. Among them, nanotubes with a one-dimensional hollow structure offer particularly large surface areas, high light absorption and fast electron transport to optimize photocatalytic performance.

Beyond controlling its morphology, the proper doping of g-C_3N_4 is critical to adjust its band structure and charge carrier concentration towards enhancing light absorption and promoting charge injection.[25,26] Dopants such as oxygen and phosphorus can not only adjust the valence band structure of the catalyst and improve the separation efficiency of photogenerated electrons and holes, but also improve the selectivity of the OER toward the two-electron pathway.[27,28]

The introduction of a co-catalyst on the surface of g-C_3N_4 is an effective strategy to improve photocatalytic performance by increasing the charge separation ability. Various noble metal co-catalyst, such as Pt, Pd, Au, have been demonstrated to promote hydrogen evolution performance.[29–33] Nevertheless, the high cost of noble metals and the moderate H_2O_2 production rates reached limit the cost-effectiveness of the process. Thus, the development of co-catalysts based on abundant and low-cost elements, such as MoS_2, Ni, NiP or CoP, [34–37] that provide an efficient and high rate photocatalytic H_2O_2 production is highly desirable.

In this study, we detail the synthesis of hollow tubular g-C_3N_4 (tCN), demonstrate their controlled oxygen doping (OtCN), and describe their surface modification with highly dispersed nickel nanoparticles (Ni/OtCN) through a photoreduction process. Nitrogen adsorption-desorption isotherms, UV–vis absorption and photoluminescence spectroscopy, and photochemical test are used to investigate charge separation and transfer abilities. Besides, rotating ring disk electrode analysis, active species capture experiments and the DFT calculations are used to analyze the mechanism for H_2O_2 generation. With the unique 1-D hollow structure, high charge separation efficiency and excellent reaction selectivity during ORR process Ni/OtCN achieved outstanding H_2O_2 photocatalytic generation performance.

2. Experimental

2.1. Preparation of tubular g-C_3N_4 precursor (C-M)

g-C_3N_4 nanotubes were prepared by a self-assembly method using melamine (99%, Acros Organics) and cyanuric acid (99%, Acros Organics). Typically, 1 g melamine and 1 g cyanuric acid were separately added into 300 ml deionized water under stirring at 80 °C for about 10 minutes until completely dissolved. Then the melamine solution was slowly added to the cyanuric acid solution under homogeneous stirring, and let it self-assemble at 80 °C for 1.5 hours. The product was centrifuged and washed twice with 80 °C deionized water to remove the unassembled melamine and cyanuric acid. The filtered product was re-dispersed in deionized water and then settled at room temperature for 12 hours. Then the supernatant was removed to obtain a flocculent precipitate. The precipitate was then freeze-dried for 48 hours to obtain the g-C_3N_4 precursor that we will refer to as C-M.

2.2. Preparation of O-doped tubular g-C_3N_4 (OtCN) and bulk g-C_3N_4 (bCN)

The OtCN was prepared by a two-step heating process. In detail, 2 g C-M was introduced into a lidded porcelain crucible and calcined at 520 °C for 2h with a temperature increase rate of 2 $°C\cdot min^{-1}$ under Ar atmosphere. Then the product was mixed with the proper amount (0 g, 200 mg, 400 mg, 600 mg, or 800 mg) of ammonium persulfate (98%, Sigma) and calcined again at 520 °C for 2h with a temperature ramp of 5 $°C\cdot min^{-1}$. The products were named O_xtCN, with x=0, 0.1, 0.2, 0.3, or 0.4 for the different amounts of ammonium persulfate introduced. The bulk g-C_3N_4 (bCN) was prepared through a similar method but replacing the C-M with melamine and adding no ammonium persulfate.

2.3. Preparation of Ni/OtCN, Au/OtCN and Pt/OtCN

100 mg of OtCN was added into 100 ml deionized water containing 10 ml triethanolamine (99%, Acros Organics), 8.5 mg nickel acetate tetrahydrate (99%, Acros Organics), and 500 mg sodium hypophosphite (99%, Sigma), and the solution was sonicated for 30 min. Afterwards, argon was bubbled into the solution for 30 min to displace the oxygen. Then the solution was irradiated with UV-vis light (300 W Xe lamp) under continuous stirring and argon bubbling for 30 min. The product was centrifuged and washed 3 times with water and ethanol (90%, Acros Organics) and finally dried under vacuum for 6h. The sample was named $Ni_{2\%}$/OtCN. Samples with higher Ni concentration, Ni_x/OtCN (x=4%, 6% and 8%), were prepared using the same procedure but adding the proper higher amount of nickel acetate. Au/OtCN and Pt/OtCN samples were also prepared by this photo-deposition method using $H_2PtCl_6 \cdot 6H_2O$ (99%, Acros Organics) and $HAuCl_4 \cdot 4H_2O$ (99%, Acros Organics) precursors and irradiating the samples with UV light for 1 h.

3. Results and discussions

3.1. Structural and chemical properties of oxygen-doped tubular g-C_3N_4 and the Ni-loaded composite

Oxygen-doped tubular carbon nitride samples loaded with Ni nanocrystals (Ni/OtCN) were obtained through a 4-step process involving the synthesis of the carbon nitride precursor from the combination of melamine and cyanuric acid in water, annealing under argon at 520 °C, oxygen doping using ammonium persulfate, and photo-deposition of Ni (Figure 1).

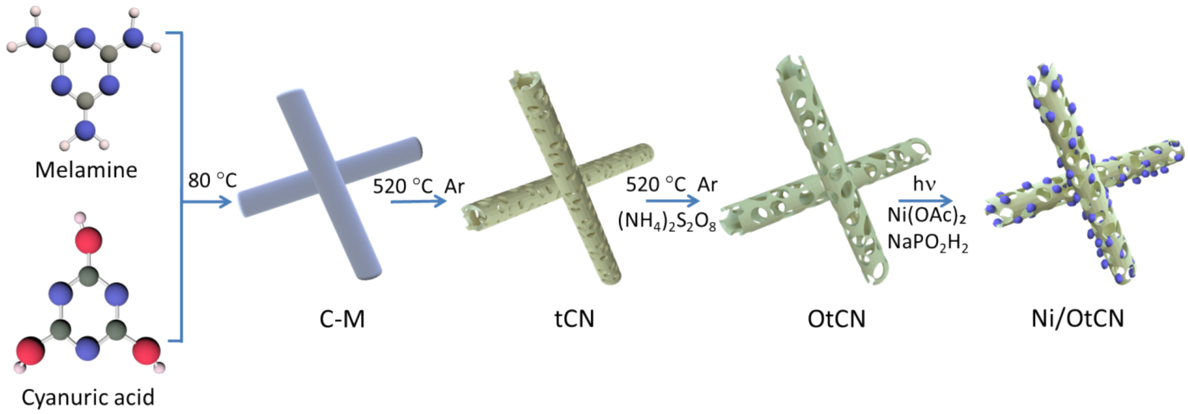

Figure 1. Schematic illustration on the synthesis of Ni/OtCN samples.

Because the water solubility of melamine and cyanuric acid is very low at room temperature, the two components were dissolved at 80 °C to ensure their full and uniform dispersion before self-assembly. The assembly is driven by the hydrogen bond formation between the amino group on melamine and the hydroxyl group on cyanuric acid. To determine the optimum precursor composition, materials with different melamine and cyanuric acid molar ratios (1:2, 1:1 and 2:1) were prepared for comparison. SEM analysis of the obtained precursors (Figures 2a and S1) showed the 1:1 ratio to provide the best-defined nanorod structures, with a diameter in the range 300-600 nm and lengths of 15-30 μm. This result is consistent with the equal number of functional groups of both molecules, thus assembling at a 1:1 molar ratio. While the 1:2 and 2:1 ratios also resulted in nanorod-like structures, they showed poor uniformity and presented a large amount of unassembled precursor on their surfaces.

Once the self-assembly process was completed, the material was washed with hot water to remove the residual not-assembled precursors. To prevent agglomerating during the drying process, samples were freeze-dried, which yielded dried materials with high porosity, as observed in Figure S2. The freeze-drying step was demonstrated as particularly important because an extensive agglomeration of the nanorods results in a high sintering and very notable loss of porosity during the posterior annealing step at 520 °C.

To minimize the damage to the nanostructure during the thermal polymerization of the C-M precursor, the annealing and oxygen doping of the material was divided into two steps. The first annealing step at 520 °C used a relatively low heating rate of 2 °C·min^{-1}. After this step, samples were combined with a proper amount of ammonium persulfate and the mixture was annealed again at 520 °C for two additional hours using a temperature ramp of 5 °C·min^{-1}. This second annealing step completed the polymerization process. Besides, during the annealing process, the ammonium persulfate releases ammonia, sulfur dioxide, and oxygen, which partially react with the polymerizing carbon nitride thus regulating its surface oxygen content. After the two-step thermal polymerization at 520 °C, the nanorod precursor was turned into g-C_3N_4 nanotubes that maintained approximately the same size as the precursor nanorods (Figure 2b).

The annealed and oxygen-doped samples, OtCN, were dispersed in a solution containing nickel acetate tetrahydrate to be loaded with nickel nanoparticles through a photodeposition process. As a result, as observed in Figure 2c, uniformly and highly dispersed Ni nanoparticles were grown on the surface of the OtCN. Figure S3 provides results from the EDX analysis of $Ni_{4\%}/O_{0.2}$tCN showing the weight percentage of O and Ni to be 2.1 % and 3.2 %, respectively.

TEM analysis of OtCN samples confirmed the tubular structure of the products and further showed the nanotube walls to have a porous structure (Figure 2d). The tubular structure of OtCN was thus significantly different from that of bulk g-C_3N_4 (bCN) produced from directly annealing the melamine (Figure S5a). TEM images of the Ni/OtCN samples also confirmed the homogeneous distribution of Ni nanoparticles and showed their size to be in the range 20-60 nm (Figure 2e). HRTEM micrographs revealed that the selected nanoparticles had a crystal phase matching the Ni cubic phase (space group=FM3-M) with a=b=c=3.5241 Å. (Figure 2f). EELS chemical composition maps obtained on the Ni/OtCN nanotubes displayed a uniform distribution of O, N and C and the presence of Ni-rich regions corresponding to the Ni nanoparticles.

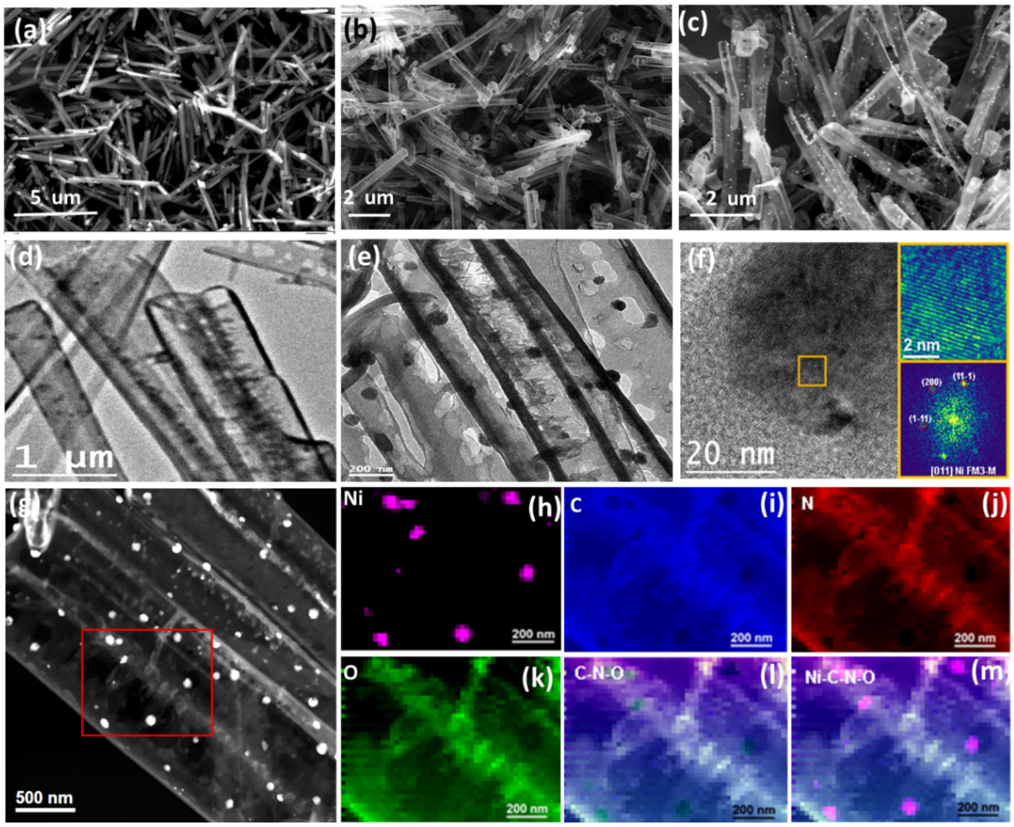

Figure 2. (a) SEM image of the C-M precursor. (b) SEM image of OtCN. (c) SEM image of Ni/OtCN. (d) TEM image of OtCN. (e) TEM image of Ni/OtCN. (f) HRTEM micrograph obtained on a representative region of the Ni/OtCN nanostructures. On the top right, we show a magnified detail (top right) of the orange squared region in the HRTEM image and its corresponding indexed power spectrum (bottom right) which reveals that this nanoparticle has a crystal phase in agreement with the Ni cubic phase (space group=FM3-M) with a=b=c=3.5241 Å, visualized along its [011] zone axis. (g) HAADF STEM general detail of the Ni/OtCN catalyst, showing the presence of Ni nanoparticles as bright spots. EELS chemical composition maps were obtained on the red squared area of the STEM micrograph. Individual composition maps were obtained by using: (h) Individual Ni $L_{2,3}$-edges at 855 eV (pink), (i) C K-edges at 284 eV (blue), (j) N K-edges at 401 eV (red) and (k) O K-edges at 532 eV (green), as well as their composites for C-N-O and Ni-C-N-O.

Figure 3a displays the XRD patterns of $O_{0.2}$tCN, $Ni_x/O_{0.2}$tCN and a reference bCN. The main diffraction peaks at about 13.1° and 27.4° observed from all the samples are assigned to the (100) and (002) family planes of g-C_3N_4, respectively. Compared with bCN, the (002) peak of OtCN samples shows a slight shift from 27.4° to 27.2° which is a signature of an increase of the interplanar distance associated with the presence of oxygen.[38,39] Besides, the (002) diffraction peak of OtCN is broader and weaker than that of bCN, which is attributed to the tubular structure of OtCN. The samples containing Ni show no alteration of the g-C_3N_4 diffraction peaks compared with OtCN, which indicates that the loading of Ni has no effect on the OtCN structure. Meanwhile, Ni/OtCN samples display two additional XRD peaks at 44.3° and 51.5° that are assigned to the (111) and (200) family planes of cubic nickel. The intensity of these peaks correlates with the amount of Ni introduced, proving the successful loading of controlled amounts of nickel.

FTIR spectroscopy was used to gain further insight into the structure of the material. As shown in Figure 3b, all OtCN materials displayed the fingerprints of g-C_3N_4, including the absorption peak at 812 cm^{-1} that corresponds to the out-of-plane bending of the triazine units, and the range of peak at 1200–1600 cm^{-1} that are related to the stretching modes of C-N in the aromatic heterocyclic rings. Besides, OtCN samples displayed FTIR peaks at 1235 and 1075 cm^{-1}, which intensity increased with the amount of ammonium persulfate used during the synthesis. These peaks are associated with the stretching mode of C-O-C group.[27,40]

Figure 3c displays the UV–vis diffuse reflectance spectra of the different samples. The absorption edge of OtCN samples presented an obvious red-shift compared with bCN. This redshift was accentuated with the increase of the oxygen content. As shown in Figure 3d, the band gaps of bCN and OtCN samples, calculated according to Kubelk-Munk function, shifted from 2.73 eV for bCN, to 2.56 eV for $O_{0.4}$tCN. Besides, the presence of oxygen resulted in a notable enhancement of the Urbach tail, which is associated with the presence of defects as a result of oxygen doping.[27,39] As expected from the metallic character of the introduced Ni nanoparticles, the Ni/OtCN composites presented a strong absorption in the visible range of the spectra, which was enhanced with the increasing contents of Ni, from 2 to 8%. On the other hand, the presence of Ni did not result in a shift of the OtCN absorption edge.

Mott-Schottky analysis was used to further investigate the band structure of the samples (Figure S4). The flat band potentials of bCN and OtCN were obtained from the fitting of the Mott-Schottky plots and were used to estimate the position of the conduction band minimum (assuming it is ca. 0.1 eV above the flat band)[41][42] and valence band maximum (considering $E_g = E_{vb} - E_{cb}$).[43] Figure 3e displays the schematized band structure experimentally determined from bCN and OtCN samples.

Figure 3f displays the nitrogen adsorption-desorption isotherms of bCN and $O_{0.2}$tCN nanotubes. Both samples exhibit type IV isotherms with H3 hysteresis loops, indicating the presence of a mesoporous structure. As shown in Table S1, the specific surface area (SSA) of $O_{0.2}$tCN nanotubes was 124 $m^2 \cdot g^{-1}$, which is over six-fold larger than that of bCN (18.7 $m^2 \cdot g^{-1}$). The calculated pore size distribution of the two samples is shown in Figure S5b. As expected from SEM images, the pore volume of OtCN, 0.97 $cm^3 \cdot g^{-1}$, was significantly larger than that of bCN, 0.19 $cm^3 \cdot g^{-1}$.

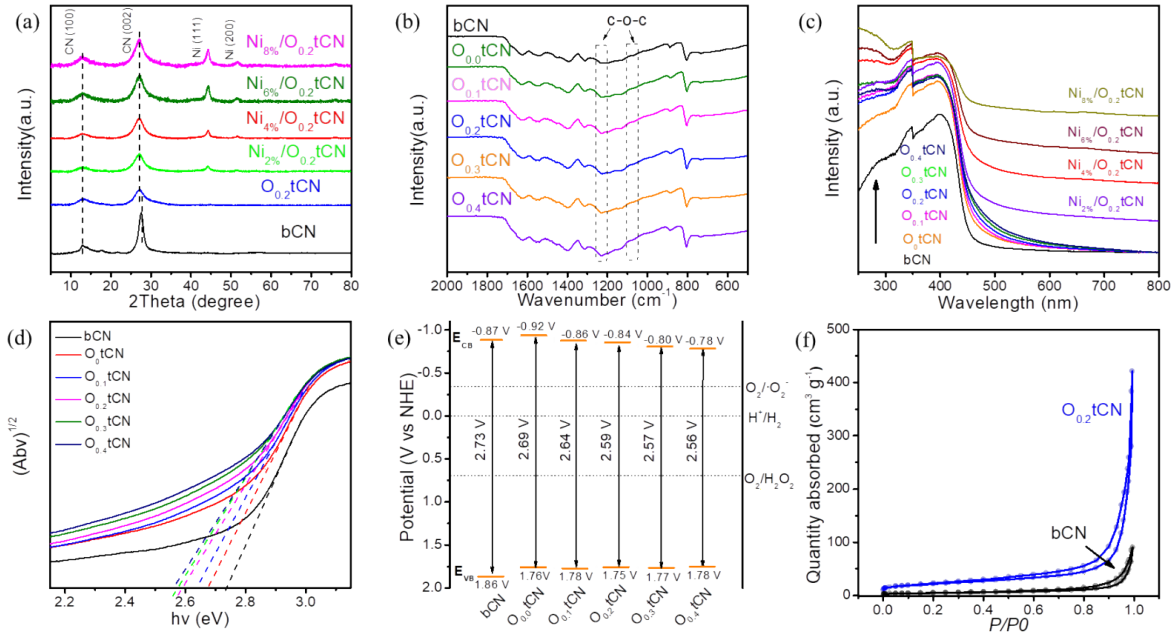

Figure 3. (a) XRD pattern of bCN ,$O_{0.2}$tCN and $Ni_x/O_{0.2}$tCN (x=2%, 4%, 6% and 8%). (b) FTIR spectra of bCN and O_xtCN. (c) UV–Vis absorption spectra of bCN, O_xtCN and $Ni_x/O_{0.2}$tCN. (d) plot of the band energy spectra and (e) band structure alignments for the bCN and OtCN samples. (f) N_2 adsorption-desorption isotherms of bCN and $O_{0.2}$tCN.

Figure 4 displays the XPS spectra of bCN, $O_{0.2}$tCN, and $Ni_{4\%}/O_{0.2}$tCN samples. The high-resolution C 1s XPS spectra showed three main contributions at 288.2 eV, 286.5 eV, and 284.8 eV, which were assigned to C-(N_3), C–NH_X and C–C/C=C, respectively.[40] Besides, the OtCN samples displayed a fourth C 1s peak 288.5 eV corresponding to C-O obtained from the replacement of N atoms by O in the CN heterocycles. All samples displayed the presence of oxygen at their surface, including the bCN. The high-resolution O 1s XPS spectrum of bCN was fitted with two peaks at 531.7 eV and 533.1 eV, which were associated with adsorbed oxygen-containing species such as water, O_2, OH^- groups and even CO_2. [38] Besides, samples OtCN and Ni/OtCN displayed an additional contribution at 530.7 eV which is assigned to the C-O bond. Additionally, a peak at 529.7 eV was identified in the XPS spectrum of Ni/OtCN, and it was assigned to oxygen within a nickel oxide chemical environment created by the surface oxidation of the Ni nanoparticles. The high-resolution N 1s XPS spectra of bCN, $O_{0.2}$tCN and $Ni_{4\%}/O_{0.2}$tCN was fitted with three peaks at binding energies of 398.1 eV, 499.4 eV, and 400.5 eV, which were assigned to N-(C_2), N-(C_3) and N-H_x groups of the heptazine framework, respectively. Finally, the high-resolution Ni 2p XPS spectrum of Ni/OtCN was fitted with three doublets, corresponding to metallic Ni ($2p_{3/2}$ at 851.6 eV), Ni $^{2+}$ ($2p_{3/2}$ at 855.8 eV) and a Ni $^{2+}$ shake-up satellite ($2p_{3/2}$ at 860.4 eV).[44]

The EPR spectra of bCN and OtCN samples are displayed in Figure 4f. The Lorentzian absorption line at g =2.0027 is a fingerprint of the unpaired electrons of the sp^2 hybridized C atoms in the aromatic rings.[27,38] The EPR signal of the OtCN sample is significantly less intense than that of bCN, which is consistent with the partial replacement N by O atoms, thus decreasing the number of lone pair electrons. Overall, the above experimental results confirmed the presence of O within OtCN replacing N atoms.

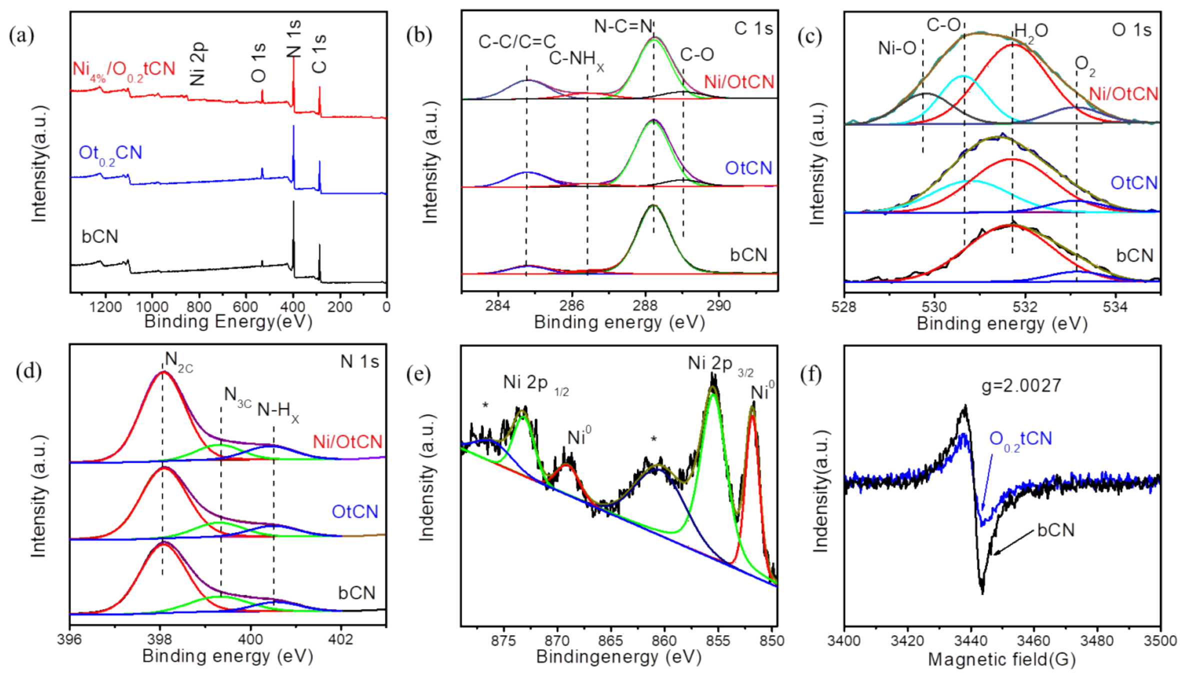

Figure 4. (a) XPS survey spectra. (b-d) High-resolution XPS spectra of (b) C 1s, (c) O 1s and (d) N 1s obtained from bCN, $O_{0.2}$tCN and $Ni_{4\%}/O_{0.2}$tCN samples. (e) Ni 2p XPS spectrum of $Ni_{4\%}/O_{0.2}$tCN. (f) EPR spectra of bCN and $O_{0.2}$tCN.

3.2. Photocatalytic H_2O_2 evolution

Figure 5a displays the photocatalytic H_2O_2 generation from bCN, $O_{0.2}$tCN, and $Ni_{4\%}/O_{0.2}$tCN irradiated during 2h with visible light (λ > 420 nm). The H_2O_2 production rate of $O_{0.2}$tCN was fourfold higher than that of bCN (Figure 5b). Besides, when loading the $O_{0.2}$tCN with Ni, the H_2O_2 evolution rate further increased to reach nearly an order of magnitude higher values than bCN. Besides the Ni/OtCN sample displayed higher H_2O_2 evolution rates than noble metal co-catalyst: Au/OtCN and Pt/OtCN. The presence of Au showed an obvious improvement over OtCN, but the presence of Pt had no positive impact on the H_2O_2 generation, which is associated with a low two-electron reaction selectivity and a high H_2O_2 decomposition rate during the oxygen reduction reaction.

To find the optimal amount of oxygen doping, O_XtCN samples produced using different amounts of ammonium persulfate were tested (Figure S7a-b). O_XtCN samples containing relatively small amounts of oxygen ($0 < x < 0.4$) exhibited a significant enhancement of the H_2O_2 generation rate over tCN, but too high oxygen substitutions resulted in a lower H_2O_2 evolution rate. Among all the O_xtCN samples, $O_{0.2}$tCN displayed the best H_2O_2 generation performance, 58.1 μmol·h $^{-1}$.

The amount of Ni was optimized by measuring the photocatalytic hydrogen peroxide generation on $Ni_x/O_{0.2}$tCN containing different Ni concentrations (Figure S7c-d). The loading of $O_{0.2}$tCN with a moderate amount of Ni nanoparticles largely enhanced the photocatalytic performance toward H_2O_2 generation. At a Ni loading of 2% and 4%, the H_2O_2 generation rate was improved to 88.2 μmol·h $^{-1}$ and 123.2 μmol·h $^{-1}$, which is 1.5 and 2.1 times higher than that of $O_{0.2}$tCN, respectively. When further increasing the Ni loading to 6% and 8% the H_2O_2 production rate decreased to 101 μmol·h $^{-1}$ and 75 μmol·h $^{-1}$, respectively. This decrease of the H_2O_2 production rate at high Ni loads may be related to the aggregation of small Ni particles and the blocking of the visible light absorption of the C_3N_4 caused by an excess of Ni.

As displayed in Figure 5c, control experiments demonstrated that the presence of O_2 and light irradiation were required for the H_2O_2 generation, but the $Ni_{4\%}/O_{0.2}$tCN sample was able to achieve a notable photocatalytic H_2O_2 generation rate even in the absence of ethanol as a sacrificial agent. Besides, as shown in Fig. S8, $Ni_{4\%}/O_{0.2}$tCN also shows a prominent photocatalytic hydrogen peroxide generation performance of about 5012 μmol g^{-1}·h^{-1} under simulated solar light, using an AM1.5 filter.

The apparent quantum yield (AQY) of the process was evaluated under 380 nm (0.53 mW·cm^{-2}), 420 nm (9.91 mW·cm^{-2}) and 600 nm (17.66 mW·cm^{-2}) irradiation (Figures 5d and S8, and Table S2, see details in the SI). For $Ni_{4\%}/O_{0.2}$tCN, the AQY at 380 nm and 420 nm was estimated at 28.2% and

14.9%, respectively. Even under 600 nm light irradiation, an AQY of 0.7% was achieved for $Ni_{0.4}/O_{0.2}tCN$, which is consistent with UV-vis spectroscopy results (Figure 5d).[45]

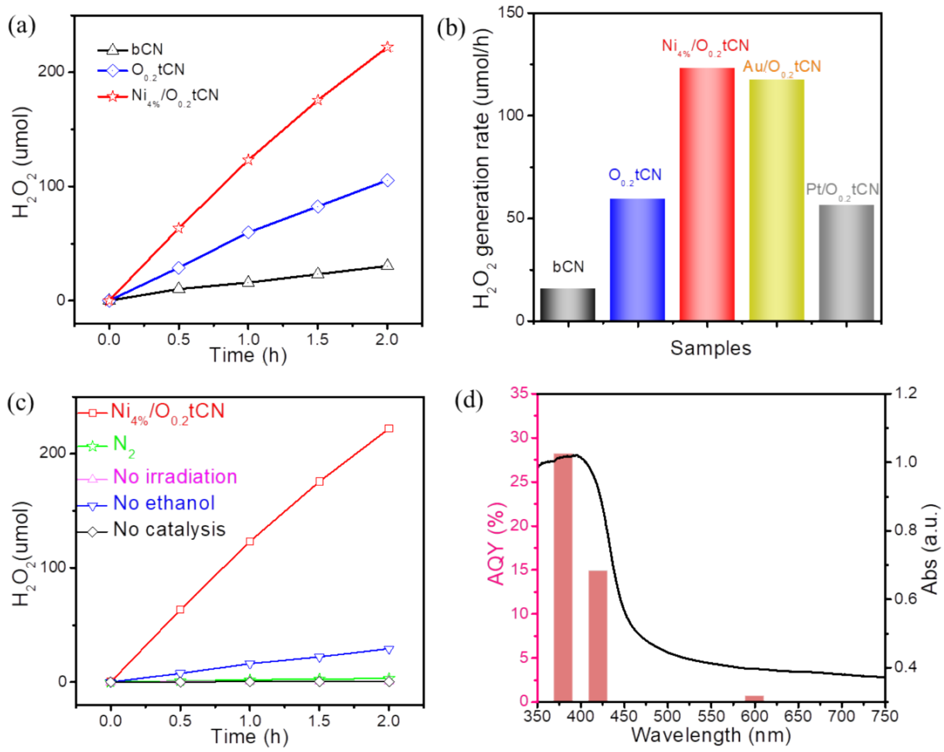

Figure 5. (a) Photocatalytic hydrogen peroxide generation on bCN, $O_{0.2}tCN$ and $Ni_{4\%}/O_{0.2}tCN$ during two hours under visible light illumination (λ > 420 nm). (b) Photocatalytic hydrogen peroxide generation rate of bCN, $O_{0.2}tCN$, $Ni_{4\%}/O_{0.2}tCN$, $Au_{4\%}/O_{0.2}tCN$ and $Pt_{4\%}/O_{0.2}tCN$ (c) H_2O_2 production on $Ni_{4\%}/O_{0.2}tCN$ under different conditions including the use of N_2 instead of O_2, no irradiation, no ethanol and no photocatalyst. (d) Wavelength-dependent AQY of $Ni_{4\%}/O_{0.2}tCN$.

3.3. Charge carrier dynamics

The electrochemical characterization of the samples allowed further study of their charge transfer and transport properties. As observed in Figure 6a, bCN, $O_{0.2}tCN$ and $Ni_{4\%}/O_{0.2}tCN$ electrodes showed positive photocurrents under visible-light irradiation. Among them, $O_{0.2}tCN$ showed a slightly higher photocurrent density than bCN, but the highest photocurrents were obtained with the $Ni_{4\%}/O_{0.2}tCN$ electrode, reaching about 7.2 and 4 times higher current densities than with bCN and $O_{0.2}tCN$, respectively. These results demonstrate that $O_{0.2}tCN$ and especially the presence of Ni nanoparticles significantly increase the charge separation and transfer efficiency, which is in good agreement with the photocatalysis results. [46]

Charge transfer and transport properties were further evaluated by electrochemical impedance spectroscopy (EIS). Figure 6b displays the Nyquist plot of the impedance spectra for the different materials. The larger arc associated with the transfer resistance of photo-generated charges[37] has a significantly smaller diameter for $O_{0.2}$tCN than bCN, indicating a faster charge transfer efficiency in the former. Besides, the sample containing Ni, $Ni_{4\%}/O_{0.2}$tCN, presents a much smaller arc radius than the other two samples, confirming the much lower charge transfer resistance in the presence of Ni.

The photoluminescence (PL) spectra of the different samples under 300 nm light excitation is displayed in Figure 6c. The bCN sample displayed a broad and intense PL band at ca. 455 nm, which is associated with the radiative band-to-band recombination of photogenerated charge carriers within C_3N_4. With oxygen doping, the PL intensity significantly decreases owing to the presence of oxygen-related non-radiative recombination centers. Besides, the presence of Ni introduces additional recombination sites which further quenches the C_3N_4 PL. As obtained from time-resolved PL (TRPL) spectroscopy (Figure 6d) and consistently with previous results, $O_{0.2}$tCN and $Ni_{4\%}/O_{0.2}$tCN samples exhibited much shorter average PL lifetimes (4.06 ns and 3.39 ns) than bCN (6.22 ns), demonstrating the strong electronic effect of the substitutional oxygen and nickel nanoparticles.[36][47]

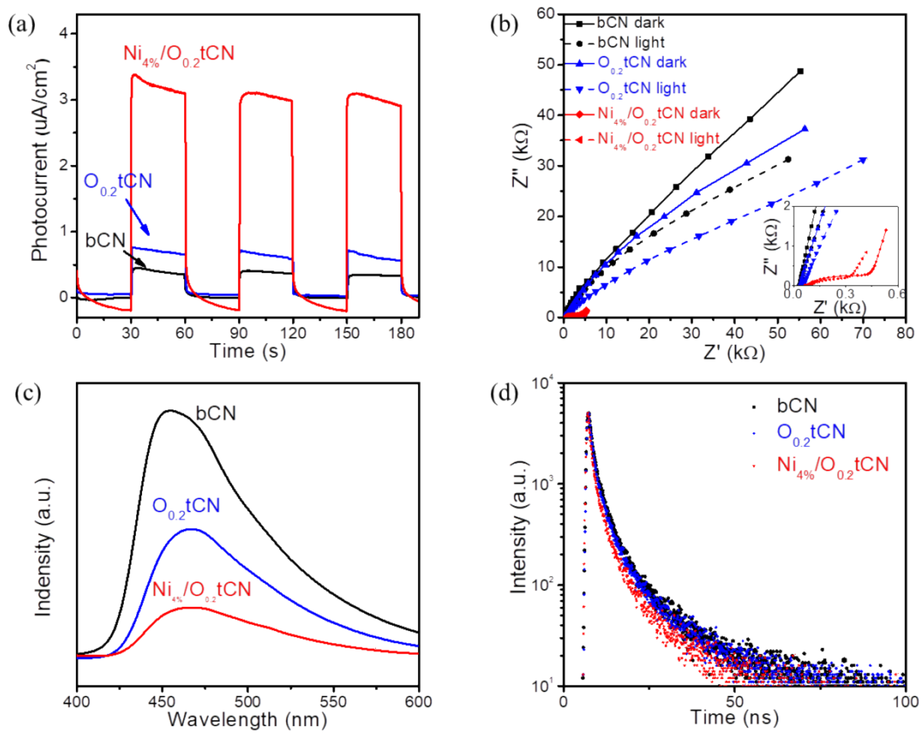

Figure 6. (a) Photocurrent response curves of bCN ,$O_{0.2}$tCN and $Ni_{4\%}/O_{0.2}$tCN; (b) Electrochemical impedance

spectroscopy (EIS) Nyquist plots of bCN ,$O_{0.2}$tCN and $Ni_{4\%}$/$O_{0.2}$tCN; (c,d) Plspectra and TRPL decay of bCN ,$O_{0.2}$tCN and $Ni_{4\%}$/$O_{0.2}$tCN.

3.4. Reaction mechanism

The generation of H_2O_2 from the coupling of the oxygen reduction reaction (ORR) with the oxidation of an alcohol takes place through two main pathways. Both paths share the alcohol dehydrogenation reaction as hole-scavenging process and the oxygen adsorption as the initial ORR step:

$$RCH_2OH + 2h^+ \rightarrow RCHO + 2H^+ \quad (1)$$

$$O_2 + * \dashrightarrow *O_2 \quad (2)$$

In one possible path, the reduction of the adsorbed oxygen molecule ($*O_2$) can take place through a direct two-electron route:

$$*O_2 + 2H^+ + 2e^- \rightarrow H_2O_2 \quad (3)$$

The second possible ORR pathway is a two-step single-electron process, that can be deglosed as follows:

$$*O_2 + e^- \rightarrow *O_2^- \quad (3)$$

$$*O_2^- + H^+ \rightarrow *HOO \quad (4)$$

$$*HOO + e^- \rightarrow HOO^- \quad (5)$$

$$HOO^- + H^+ \rightarrow H_2O_2 \quad (6)$$

Besides, the H_2O_2 evolution reaction competes with the oxygen reduction to H_2O, which overall involves a total of $4e^-$ (see details in the SI):

$$O_2 + 4H^+ + 4e^- \rightarrow 2H_2O \quad (7)$$

To electrochemically determine the selectivity of the catalyst toward the production of H_2O_2 instead of H_2O, one can estimate the electron transfer number (n) of the ORR reaction. The closer the electron transfer number is to 2, the higher the H_2O_2 generation efficiency. A rotating ring-disk electrode (RRDE) was used to estimate n, and thus assess the ORR pathway and H_2O_2 generation efficiency. Within an RRDE, the peroxide species produced at the disk electrode are detected by the ring electrode. Thus, n can be determined from the ratio of the ring current (I_r) and the disk current

(I_d) using the following equation:

$$\mathrm{n} = 4\frac{I_d}{I_d + I_r/N} \tag{8}$$

where N is the collection efficiency of the ring electrode, which is estimated at 0.42 (see details in the SI).[48] Besides, the percentage of H_2O_2 produced can be determined from:

$$\%HOO^- = 200 \times \frac{I_r/_N}{I_d + I_r/_N} \tag{9}$$

The disk electrode was scanned cathodically at a scan rate of 10 mV·s^{-1}, while the ring potential was set at 0.5 V vs. Ag/AgCl (Figure 7). The linear sweep voltammetry (LSV) curves of bCN achieved I_r = 0.40 mA·cm^{-2} and I_d=-1.91 mA·cm^{-2} at -1.0 V vs. Ag/AgCl. From these values, a transfer number n =2.71 and an H_2O_2 selectivity of 60.8% was determined.[49] Similarly, a transfer number n = 2.32 and an H_2O_2 selectivity of 81.2% was obtained for $O_{0.2}$tCN, and n = 2.24 and an H_2O_2 selectivity of 88.9% for $Ni_{4\%}/O_{0.2}$tCN. Overall, the RRDE measurements indicated that the oxygen doping and the presence of Ni significantly promoted the two-electron pathway for oxygen reduction to H_2O_2 over the four-electron H_2O generation.

To differentiate between the one-step two-electron direct ORR ($O_2 \rightarrow H_2O_2$) and the sequential two-step single-electron indirect reduction ($O_2 \rightarrow {}^*O_2^- \rightarrow H_2O_2$) routes,[19][18] LSV curves were analyzed in more detail (Figures 7 and S10). Notice that the bCN and $O_{0.2}$tCN samples exhibit two reduction plateaus at around −0.2 V and −0.5 V, suggesting a two-step pathway for H_2O_2 generation.[19][50] As observed in Figure 7b,c, no obvious H_2O_2 current is detected in the ring electrode during the first plateau, in the potential range -0.2 V to -0.4 V. Only when reaching the second plateau a ring current is measured, which indicates the successive two single-electron reduction pathway. On the other hand, after loading the Ni nanoparticles, the first plateau almost disappears and the onset potential of the H_2O_2 current at the ring electrode approximately matches that of the disk electrode, pointing at a one-step two-electron direct reduction pathway in $Ni_{4\%}/O_{0.2}$tCN. Overall, these results indicate that the introduction of nickel transforms the reaction from a two-step single-electron process to a direct two-electron process.

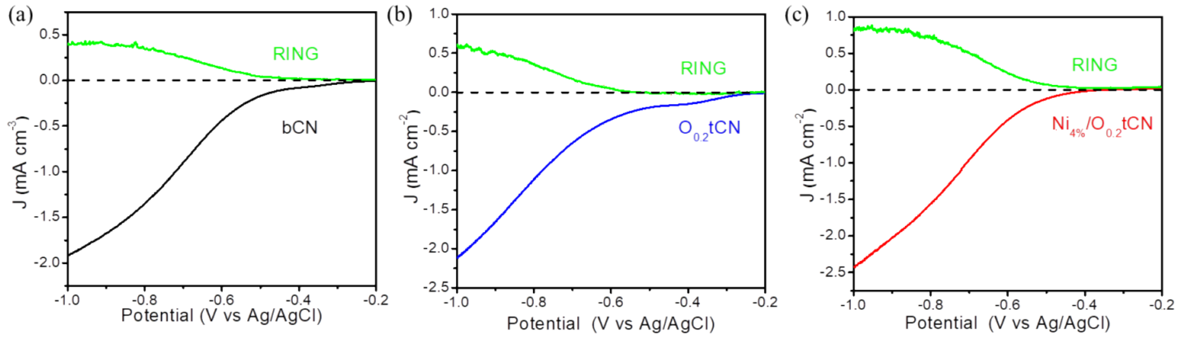

Figure 7. LSV curves of (a) bCN, (b) $O_{0.2}$tCN and (c) $Ni_{4\%}/O_{0.2}$tCN obtained using an RRDE with a rotating speed of 1600 rpm and a ring biased at 0.5 V.

DFT calculations were carried out to further understand the selectivity of the ORR process on CN, OCN and Ni/OCN. The top view of the intermediates adsorption and the free energy diagram of ORR on the three materials are shown in Figure S12 and Table S4. The bCN sample is characterized by the strongest adsorption strength of ORR intermediates, which may hamper the product formation. The reduction of *OOH and *OH to form the final products, H_2O_2 or H_2O, are generally considered as the limiting ORR steps determining the reaction rate and pathway, either $2e^-$ or $4e^-$. [17] The change of Gibbs free energy (ΔG) for the reduction of *OOH and *OH on CN was calculated to be 1.42 eV and 1.35 eV, respectively (Figure 7d). The similar ΔG for *OOH and *OH reduction on CN points toward the simultaneous occurrence of the two-electron and four-electron pathways. With the oxygen doping, ΔG for the reduction of *OOH and *OH on OCN decreased to 0.72 eV and 0.99 eV, respectively. Besides, with the introduction of Ni, ΔG values further decreased down to 0.35 eV and 0.66 eV, respectively. The lower ΔG values obtained for OCN and particularly for Ni/OCN are consistent with experimental data obtained for OtCN and Ni/OtCN. Besides, notice that the ΔG of the reduction of *OOH is significantly lower than that of *OH reduction in OCN and Ni/OCN samples, involving a higher probability of the $2e^-$ ORR pathway than the $4e^-$. These DFT calculation results are consistent with the experimental data obtained from the RRDE test, further demonstrating that the oxygen doping and the Ni loading incline the catalyst toward two-electron reactions, which can significantly improve the H_2O_2 generation efficiency.

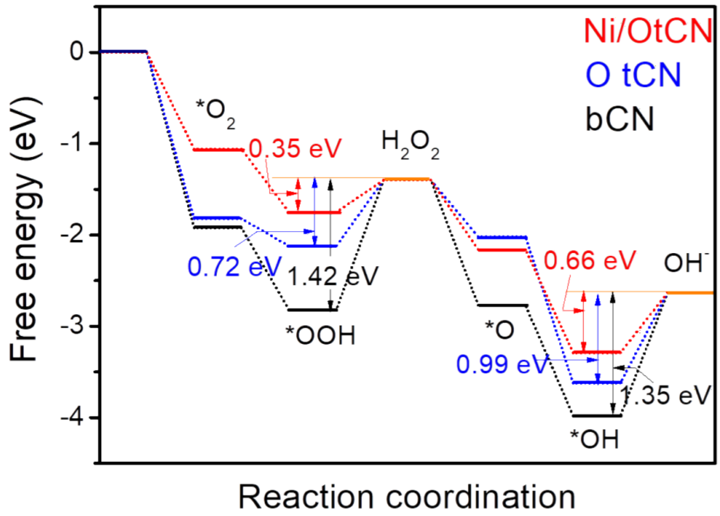

Figure 8. Free energy diagrams of oxygen reduction reaction steps on bCN, $O_{0.2}$tCN and $Ni_{4\%}/O_{0.2}$tCN

Additional experimentally of the ORR pathway were obtained by introducing a $*O^{2-}$ trapping agent in the solution, PBQ (1 mM). As shown in Figure S13a-c, after introducing the PBQ, the H_2O_2 generation rate strongly decreased for bCN and $O_{0.2}$tCN, by an 88% and 84%, respectively, demonstrating the important role played by $*O^{2-}$ as an intermediate during H_2O_2 generation process, i.e. pointing at the two-step single-electron process as the main pathway for H_2O_2 generation process in bCN and $O_{0.2}$tCN. On the contrary, the $Ni_{4\%}/O_{0.2}$tCN sample showed just a 35% decrease of H_2O_2 generation in the presence of PBQ, indicating the predominance of the two-electron process over the two single-electron processes.

To further explore the reaction mechanism and determine the role of superoxide radicals in the reaction process, DMPO spin-trapping EPR spectroscopy was used to determine the presence of $*O_2^-$ in the surface of the photocatalyst. As shown in Figure S13d, after irradiating bCN with visible light for 3 min with DMPO and methanol, four characteristic EPR features were observed. These DMPO-$*O_2^-$ characteristic EPR peaks were much more intense for the $Ot_{0.2}$CN sample under the same conditions, indicating that $O_{0.2}$tCN can generate larger amounts of $*O_2^-$ during the H_2O_2 evolution process, which is consistent with its higher H_2O_2 generation rate. On the other hand, while $Ni_{4\%}/O_{0.2}$tCN provided much higher H_2O_2 generation rates than $O_{0.2}$tCN, the $*O_2^-$ characteristic EPR signal was less intense, involving significant participation of an alternative path for H_2O_2 generation, i.e. the direct two-electron process. This result further confirms that the direct two-electron process has a fundamental role in the large H_2O_2 generation rates obtained in the presence of Ni.

Stability cycles of the $Ni_{4\%}/O_{0.2}$tCN for H_2O_2 evolution under visible-light irradiation are displayed in Figure S14a. After 8 hours of reaction, with four two-hour cycles, the catalyst maintained over 86 % photocatalytic H_2O_2 generation activities, i.e. about 106 μmol·h^{-1}, demonstrating excellent stability and reusability. Besides, SEM and XRD analysis of the catalyst after 8 h photocatalytic H_2O_2 reaction demonstrated the morphology and crystallographic structure of the material to be stable under photocatalytic reaction conditions (Figure S14b,c).

Conclusion

In summary, we detailed the synthesis of hollow tubular g-C_3N_4 (tCN), and demonstrated their controlled oxygen doping (OtCN), and their surface modification with highly dispersed nickel nanoparticles (Ni/OtCN) through a photoreduction process. OtCN samples displayed a hollow tubular structure with a large specific surface area (124 m^2·g^{-1}). With larger SSA and more porous structure OtCN can provide more reactive sites, improve the light absorption by the multiple diffusion and accelerate the diffusion of reactants and products on the surface, thereby significantly improving the photocatalytic performance. OtCN samples displayed a lower bandgap (2.59 eV) associated to the presence of oxygen atoms replacing N within the OtCN structure. Thus, OtCN enabled the capture of a wider range of the solar spectrum. In addition, the addition of Ni can provide additional active reaction sites and significantly promote the separation of photogenerated carriers. Based on the DFT and RRDE results, the doping with oxygen and the presence of Ni nanoparticles greatly reduced the energy barrier for H_2O_2 generation and improved the H_2O_2 selectivity from 60.8% to 88.9%, which enabled a more effective and efficient ORR towards H_2O_2 evolution. Upon absorbing a photon of proper energy, electron-hole pairs are photogenerated in bCN and OtCN. The holes in the valence band rapidly react with the sacrificial agent while electrons in the conduction band will be involved in the ORR. At the bCN surface, only part of the electrons can selectively undergo a two-step single-electron indirect reduction ($O_2 \rightarrow {}^*O_2^- \rightarrow H_2O_2$) two-electron process to generate H_2O_2. As for $O_{0.2}$tCN, the selectivity of the two-electron process is enhanced, but still within a two-step single-electron indirect reduction process. After loading the Ni nanoparticles, the electrons on the conduction band of OtCN are transferred to the surface of Ni which has a lower Femi level and then reducing the oxygen through a one-step two-electron direct reduction ($O_2 \rightarrow H_2O_2$) route, which is more efficient for H_2O_2 generation. Thus, the introduction of Ni could transform the reaction from a two-step single-electron process to a direct two-electron process which is more efficient and high yield. Efficient charge separation and high selective formation of H_2O_2 during ORR process allow $Ni_{4\%}/O_{0.2}tCN$ to achieve an outstanding production rate up to 2464 μmol $g^{-1} \cdot h^{-1}$ under visible light and 5021 μmol $g^{-1} \cdot h^{-1}$ under simulated solar light and AQY of 28.2% at 420 nm and 14.9% at 420 nm.

Acknowledgements

This work was supported by the European Regional Development Funds and by the Spanish Ministerio de Economía y Competitividad through the project ENE□□□□-□□□□□-C□-□-R, and ENE□□□□-□□□□□-C□. C.Q.Z., R.F.D., K.X., D.W.Y., T.Z., and X.W. thank the China Scholarship Council for the scholarship support. The authors acknowledge funding from Generalitat de Catalunya □□□□ SGR □□□ and □□□□ SGR □□□□. ICN□ acknowledges the support from the Severo Ochoa Programme (MINECO, grant no.

SEV-□□□□-□□□□) and was funded by the CERCA Programme/Generalitat de Catalunya. J.L. is a Serra Húnter Fellow and is grateful to MICINN/ FEDER RTI□□□□-□□□□□□-B-C□□, GC □□□□ SGR □□□ and to ICREA Academia program

This work was supported by the European Regional Development Funds and by the Spanish Ministerio de Economía y Competitividad through the project ENE□□□□-□□□□□-C□-□-R, and ENE□□□□-□□□□□-C□. C.Q.Z., R.F.D., K.X., D.W.Y., T.Z., and X.W. thank the China Scholarship Council for the scholarship support. The authors acknowledge funding from Generalitat de Catalunya □□□□ SGR □□□ and □□□□ SGR □□□□. ICN□ acknowledges the support from the Severo Ochoa Programme (MINECO, grant no. SEV-□□□□-□□□□) and was funded by the CERCA Programme/Generalitat de Catalunya. J.L. is a Serra Húnter Fellow and is grateful to MICINN/ FEDER RTI□□□□-□□□□□□-B-C□□, GC □□□□ SGR □□□ and to ICREA Academia program

Ruifeng Du, Ke Xiao, Xu Han, Chaoqi Zhang and Xiang Wang thank the China Scholarship Council for the scholarship support. IREC and ICN2 acknowledge funding from Generalitat de Catalunya, projects 2017 SGR 1246 and 2017 SGR 327, respectively. The authors thank the support from the project COMBENERY (PID2019-105490RB-C32) and NANOGEN (PID2020-116093RB-C43), funded by MCIN/ AEI/10.13039/501100011033/. ICN2 is supported by the Severo Ochoa program from Spanish MINECO (Grant No. SEV-2017-0706) and is funded by the CERCAProgramme / Generalitat de Catalunya. Baoying Li and Jianbin Chen greatly appreciate the financial support from the National Natural Science Foundation of China (Nos. 22171154 & 21801144), the Youth Innovative Talents Recruitment and Cultivation Program of Shandong Higher Education, The Project Supported by the Foundation (No. ZZ20190312) of State Key Laboratory of Biobased Material and Green Papermaking, Qilu University of Technology (Shandong Academy of Sciences).

Conflict of Interest

The authors declare no conflict of interest.

Reference

[1] Y. Kofuji, Y. Isobe, Y. Shiraishi, H. Sakamoto, S. Tanaka, S. Ichikawa, T. Hirai, Carbon Nitride–

Aromatic Diimide–Graphene Nanohybrids: Metal-Free Photocatalysts for Solar-to-Hydrogen Peroxide Energy Conversion with 0.2% Efficiency, J. Am. Chem. Soc. 138 (2016) 10019–10025. doi:10.1021/jacs.6b05806.

[2] M. Melchionna, P. Fornasiero, M. Prato, The Rise of Hydrogen Peroxide as the Main Product by Metal-Free Catalysis in Oxygen Reductions, Adv. Mater. 31 (2019) 1802920. doi:https://doi.org/10.1002/adma.201802920.

[3] S. Yang, A. Verdaguer-Casadevall, L. Arnarson, L. Silvioli, V. Čolić, R. Frydendal, J. Rossmeisl, I. Chorkendorff, I.E.L. Stephens, Toward the Decentralized Electrochemical Production of H2O2: A Focus on the Catalysis, ACS Catal. 8 (2018) 4064–4081. doi:10.1021/acscatal.8b00217.

[4] S. Kato, J. Jung, T. Suenobu, S. Fukuzumi, Production of hydrogen peroxide as a sustainable solar fuel from water and dioxygen, Energy Environ. Sci. 6 (2013) 3756–3764.

[5] S.A. Mousavi Shaegh, N.-T. Nguyen, S.M. Mousavi Ehteshami, S.H. Chan, A membraneless hydrogen peroxide fuel cell using Prussian Blue as cathode material, Energy Environ. Sci. 5 (2012) 8225–8228. doi:10.1039/C2EE21806B.

[6] G.H. Miley, N. Luo, J. Mather, R. Burton, G. Hawkins, L. Gu, E. Byrd, R. Gimlin, P.J. Shrestha, G. Benavides, J. Laystrom, D. Carroll, Direct NaBH4/H2O2 fuel cells, J. Power Sources. 165 (2007) 509–516. doi:https://doi.org/10.1016/j.jpowsour.2006.10.062.

[7] S. Fukuzumi, Production of liquid solar fuels and their use in fuel cells, Joule. 1 (2017) 689–738.

[8] H. Hou, X. Zeng, X. Zhang, Production of hydrogen peroxide by photocatalytic processes, Angew. Chemie Int. Ed. 59 (2020) 17356–17376.

[9] Y. Shiraishi, T. Takii, T. Hagi, S. Mori, Y. Kofuji, Y. Kitagawa, S. Tanaka, S. Ichikawa, T. Hirai, Resorcinol–formaldehyde resins as metal-free semiconductor photocatalysts for solar-to-hydrogen peroxide energy conversion, Nat. Mater. 18 (2019) 985–993.

[10] D. Tsukamoto, A. Shiro, Y. Shiraishi, Y. Sugano, S. Ichikawa, S. Tanaka, T. Hirai, Photocatalytic H2O2 Production from Ethanol/O2 System Using TiO2 Loaded with Au–Ag Bimetallic Alloy Nanoparticles, ACS Catal. 2 (2012) 599–603. doi:10.1021/cs2006873.

[11] M. Teranishi, S. Naya, H. Tada, In situ liquid phase synthesis of hydrogen peroxide from molecular oxygen using gold nanoparticle-loaded titanium (IV) dioxide photocatalyst, J. Am. Chem. Soc. 132 (2010) 7850–7851.

[12] H. Ou, C. Tang, X. Chen, M. Zhou, X. Wang, Solvated electrons for photochemistry syntheses using conjugated carbon nitride polymers, ACS Catal. 9 (2019) 2949–2955.

[13] S. Zhao, T. Guo, X. Li, T. Xu, B. Yang, X. Zhao, Carbon nanotubes covalent combined with graphitic carbon nitride for photocatalytic hydrogen peroxide production under visible light, Appl. Catal. B Environ. 224 (2018) 725–732.

[14] H. Hirakawa, S. Shiota, Y. Shiraishi, H. Sakamoto, S. Ichikawa, T. Hirai, Au nanoparticles supported on BiVO4: effective inorganic photocatalysts for H2O2 production from water and O2 under visible light, ACS Catal. 6 (2016) 4976–4982.

[15] J. Luo, Y. Liu, C. Fan, L. Tang, S. Yang, M. Liu, M. Wang, C. Feng, X. Ouyang, L. Wang, L. Xu, J. Wang, M. Yan, Direct Attack and Indirect Transfer Mechanisms Dominated by Reactive Oxygen Species for Photocatalytic H2O2 Production on g-C3N4 Possessing Nitrogen Vacancies, ACS Catal. 11 (2021) 11440–11450. doi:10.1021/acscatal.1c03103.

[16] Q. He, B. Viengkeo, X. Zhao, Z. Qin, J. Zhang, X. Yu, Y. Hu, W. Huang, Y. Li, Multiscale structural engineering of carbon nitride for enhanced photocatalytic H2O2 production, Nano Res. (2021). doi:10.1007/s12274-021-3882-1.

[17] Y. Zhao, P. Zhang, Z. Yang, L. Li, J. Gao, S. Chen, T. Xie, C. Diao, S. Xi, B. Xiao, Mechanistic analysis of multiple processes controlling solar-driven H2O2 synthesis using engineered polymeric carbon nitride, Nat. Commun. 12 (2021) 1–11.
[18] L. Zhou, J. Feng, B. Qiu, Y. Zhou, J. Lei, M. Xing, L. Wang, Y. Zhou, Y. Liu, J. Zhang, Ultrathin g-C3N4 nanosheet with hierarchical pores and desirable energy band for highly efficient H2O2 production, Appl. Catal. B Environ. 267 (2020) 118396.
[19] S. Li, G. Dong, R. Hailili, L. Yang, Y. Li, F. Wang, Y. Zeng, C. Wang, Effective photocatalytic H2O2 production under visible light irradiation at g-C3N4 modulated by carbon vacancies, Appl. Catal. B Environ. 190 (2016) 26–35.
[20] Y. Zuo, X. Xu, C. Zhang, J. Li, R. Du, X. Wang, X. Han, J. Arbiol, J. Llorca, J. Liu, A. Cabot, SnS2/g-C3N4/graphite nanocomposites as durable lithium-ion battery anode with high pseudocapacitance contribution, Electrochim. Acta. 349 (2020) 136369. doi:https://doi.org/10.1016/j.electacta.2020.136369.
[21] X. Dang, R. Yang, Z. Wang, S. Wu, H. Zhao, Efficient visible-light activation of molecular oxygen to produce hydrogen peroxide using P doped gC 3 N 4 hollow spheres, J. Mater. Chem. A. 8 (2020) 22720–22727.
[22] X. Bai, L. Wang, R. Zong, Y. Zhu, Photocatalytic Activity Enhanced via g-C3N4 Nanoplates to Nanorods, J. Phys. Chem. C. 117 (2013) 9952–9961. doi:10.1021/jp402062d.
[23] M. Tahir, C. Cao, N. Mahmood, F.K. Butt, A. Mahmood, F. Idrees, S. Hussain, M. Tanveer, Z. Ali, I. Aslam, Multifunctional g-C3N4 Nanofibers: A Template-Free Fabrication and Enhanced Optical, Electrochemical, and Photocatalyst Properties, ACS Appl. Mater. Interfaces. 6 (2014) 1258–1265. doi:10.1021/am405076b.
[24] C. Zhang, R. Du, J.J. Biendicho, M. Yi, K. Xiao, D. Yang, T. Zhang, X. Wang, J. Arbiol, J. Llorca, Y. Zhou, J.R. Morante, A. Cabot, Tubular CoFeP@CN as a Mott–Schottky Catalyst with Multiple Adsorption Sites for Robust Lithium−Sulfur Batteries, Adv. Energy Mater. 11 (2021) 2100432. doi:https://doi.org/10.1002/aenm.202100432.
[25] S. Guo, Z. Deng, M. Li, B. Jiang, C. Tian, Q. Pan, H. Fu, Phosphorus-doped carbon nitride tubes with a layered micro-nanostructure for enhanced visible-light photocatalytic hydrogen evolution, Angew. Chemie. 128 (2016) 1862–1866.
[26] G. Liu, P. Niu, C. Sun, S.C. Smith, Z. Chen, G.Q. Lu, H.-M. Cheng, Unique electronic structure induced high photoreactivity of sulfur-doped graphitic C3N4, J. Am. Chem. Soc. 132 (2010) 11642–11648.
[27] Z. Wei, M. Liu, Z. Zhang, W. Yao, H. Tan, Y. Zhu, Efficient visible-light-driven selective oxygen reduction to hydrogen peroxide by oxygen-enriched graphitic carbon nitride polymers, Energy Environ. Sci. 11 (2018) 2581–2589.
[28] J. Cao, H. Wang, Y. Zhao, Y. Liu, Q. Wu, H. Huang, M. Shao, Y. Liu, Z. Kang, Phosphorus-doped porous carbon nitride for efficient sole production of hydrogen peroxide via photocatalytic water splitting with a two-channel pathway, J. Mater. Chem. A. 8 (2020) 3701–3707.
[29] Y. Zhu, T. Wang, T. Xu, Y. Li, C. Wang, Size effect of Pt co-catalyst on photocatalytic efficiency of g-C3N4 for hydrogen evolution, Appl. Surf. Sci. 464 (2019) 36–42.
[30] Y. Zuo, Y. Liu, J. Li, R. Du, X. Yu, C. Xing, T. Zhang, L. Yao, J. Arbiol, J. Llorca, Solution-processed ultrathin SnS2–Pt nanoplates for photoelectrochemical water oxidation, ACS Appl. Mater. Interfaces. 11 (2019) 6918–6926.
[31] B. Li, Y. Zhang, R. Du, L. Gan, X. Yu, Synthesis of Bi2S3–Au dumbbell heteronanostructures

with enhanced photocatalytic and photoresponse properties, Langmuir. 32 (2016) 11639–11645.

[32] X. Chang, J. Yang, D. Han, B. Zhang, X. Xiang, J. He, Enhancing light-driven production of hydrogen peroxide by anchoring Au onto C3N4 catalysts, Catalysts. 8 (2018) 147.

[33] G. Zuo, S. Liu, L. Wang, H. Song, P. Zong, W. Hou, B. Li, Z. Guo, X. Meng, Y. Du, Finely dispersed Au nanoparticles on graphitic carbon nitride as highly active photocatalyst for hydrogen peroxide production, Catal. Commun. 123 (2019) 69–72.

[34] H. Zhang, P. Zhang, M. Qiu, J. Dong, Y. Zhang, X.W. (David) Lou, Ultrasmall MoOx Clusters as a Novel Cocatalyst for Photocatalytic Hydrogen Evolution, Adv. Mater. 31 (2019) 1804883. doi:https://doi.org/10.1002/adma.201804883.

[35] A. Indra, P.W. Menezes, K. Kailasam, D. Hollmann, M. Schröder, A. Thomas, A. Brückner, M. Driess, Nickel as a co-catalyst for photocatalytic hydrogen evolution on graphitic-carbon nitride (sg-CN): what is the nature of the active species?, Chem. Commun. 52 (2016) 104–107.

[36] X. Yu, R. Du, B. Li, Y. Zhang, H. Liu, J. Qu, X. An, Biomolecule-assisted self-assembly of CdS/MoS2/graphene hollow spheres as high-efficiency photocatalysts for hydrogen evolution without noble metals, Appl. Catal. B Environ. 182 (2016) 504–512.

[37] R. Du, Y. Zhang, B. Li, X. Yu, H. Liu, X. An, J. Qu, Biomolecule-assisted synthesis of defect-mediated Cd 1− x Zn x S/MoS 2/graphene hollow spheres for highly efficient hydrogen evolution, Phys. Chem. Chem. Phys. 18 (2016) 16208–16215.

[38] Y. Jiang, Z. Sun, C. Tang, Y. Zhou, L. Zeng, L. Huang, Enhancement of photocatalytic hydrogen evolution activity of porous oxygen doped g-C3N4 with nitrogen defects induced by changing electron transition, Appl. Catal. B Environ. 240 (2019) 30–38.

[39] P. Niu, L. Zhang, G. Liu, H. Cheng, Graphene-like carbon nitride nanosheets for improved photocatalytic activities, Adv. Funct. Mater. 22 (2012) 4763–4770.

[40] Y. Zhang, Z. Chen, J. Li, Z. Lu, X. Wang, Self-assembled synthesis of oxygen-doped g-C3N4 nanotubes in enhancement of visible-light photocatalytic hydrogen, J. Energy Chem. 54 (2021) 36–44.

[41] S. Zhao, X. Zhao, H. Zhang, J. Li, Y. Zhu, Covalent combination of polyoxometalate and graphitic carbon nitride for light-driven hydrogen peroxide production, Nano Energy. 35 (2017) 405–414.

[42] A. Ishikawa, T. Takata, J.N. Kondo, M. Hara, H. Kobayashi, K. Domen, Oxysulfide Sm2Ti2S2O5 as a stable photocatalyst for water oxidation and reduction under visible light irradiation (λ≤ 650 nm), J. Am. Chem. Soc. 124 (2002) 13547–13553.

[43] C. Xing, Y. Liu, Y. Zhang, J. Liu, T. Zhang, P. Tang, J. Arbiol, L. Soler, K. Sivula, N. Guijarro, Porous NiTiO 3/TiO 2 nanostructures for photocatatalytic hydrogen evolution, J. Mater. Chem. A. 7 (2019) 17053–17059.

[44] X. Xie, L. Shang, R. Shi, G.I.N. Waterhouse, J. Zhao, T. Zhang, Tubular assemblies of N-doped carbon nanotubes loaded with NiFe alloy nanoparticles as efficient bifunctional catalysts for rechargeable zinc-air batteries, Nanoscale. 12 (2020) 13129–13136.

[45] Y. Zhao, Y. Liu, J. Cao, H. Wang, M. Shao, H. Huang, Y. Liu, Z. Kang, Efficient production of H2O2 via two-channel pathway over ZIF-8/C3N4 composite photocatalyst without any sacrificial agent, Appl. Catal. B Environ. 278 (2020) 119289.

[46] Y. Fu, J. Zhao, H. Wang, H. Huang, Y. Liu, Y. Dou, M. Shao, Z. Kang, All-solid-state Z-scheme system of NiO/CDs/BiVO4 for visible light-driven efficient overall water splitting, Chem. Eng. J.

358 (2019) 134–142.

[47] Y. Li, H. Xu, S. Ouyang, D. Lu, X. Wang, D. Wang, J. Ye, In situ surface alkalinized gC 3 N 4 toward enhancement of photocatalytic H 2 evolution under visible-light irradiation, J. Mater. Chem. A. 4 (2016) 2943–2950.

[48] R. Liu, H. Liu, Y. Li, Y. Yi, X. Shang, S. Zhang, X. Yu, S. Zhang, H. Cao, G. Zhang, Nitrogen-doped graphdiyne as a metal-free catalyst for high-performance oxygen reduction reactions, Nanoscale. 6 (2014) 11336–11343. doi:10.1039/C4NR03185G.

[49] L. Hao, S. Zhang, R. Liu, J. Ning, G. Zhang, L. Zhi, Bottom-Up Construction of Triazine-Based Frameworks as Metal-Free Electrocatalysts for Oxygen Reduction Reaction, Adv. Mater. 27 (2015) 3190–3195. doi:https://doi.org/10.1002/adma.201500863.

[50] H. Kim, O.S. Kwon, S. Kim, W. Choi, J.-H. Kim, Harnessing low energy photons (635 nm) for the production of H 2 O 2 using upconversion nanohybrid photocatalysts, Energy Environ. Sci. 9 (2016) 1063–1073.